Chapter 6: The Photon Remnant In Resolved Photoproduction At HERA

Introduction

In chapter 2, it was emphasised that resolved events are expected to have a remnant from the photon whereas direct events, in which the whole photon interacts, are not. A search for this photon remnant in photoproduction events may therefore provide a means of discriminating between direct and resolved events. It is expected that resolved processes will dominate when tagged electrons are used as the electron tagger acceptance only covers the region $1\text{x}10^{-8} < Q^2 < 0.01\ \text{GeV}^2$.

Therefore, the first task of this study is to confirm the existence of the photon remnant. In the simple parton picture, one parton from the photon interacts with a parton from the proton and the other parton from the photon is left to carry the remainder of the photon's momentum. Hence, in this simple picture, the photon remnant has no transverse momentum and is lost down the beam pipe. However, as the remnant is not a colour singlet, it must be linked by colour forces to the rest of the event. This is expected to impart sufficient transverse momentum to the photon remnant to enable it to be detected. Once the existence of the photon remnant has been confirmed, its properties should be examined and compared with theoretical predictions.

Additionally, the photon remnant can provide useful information on the kinematics of the events. The normal procedure for calculating the kinematics of a photoproduction event makes use of the information about the partons using information from the final state jets. In principle, the photon remnant may be used as an independent check of x_γ, the fraction of the photon energy taken by the parton which hard scattered. When x_γ is small, the photon remnant carries most of the four-momentum of the initial photon and may therefore be easier to reconstruct than the jets.

A complication to the study is an uncertainty in how best to define the photon remnant. As an illustration of the problem, the electron side of a photoproduction event is shown in figure 6.1. It is not clear where initial state radiation from the initiator quark should be placed.

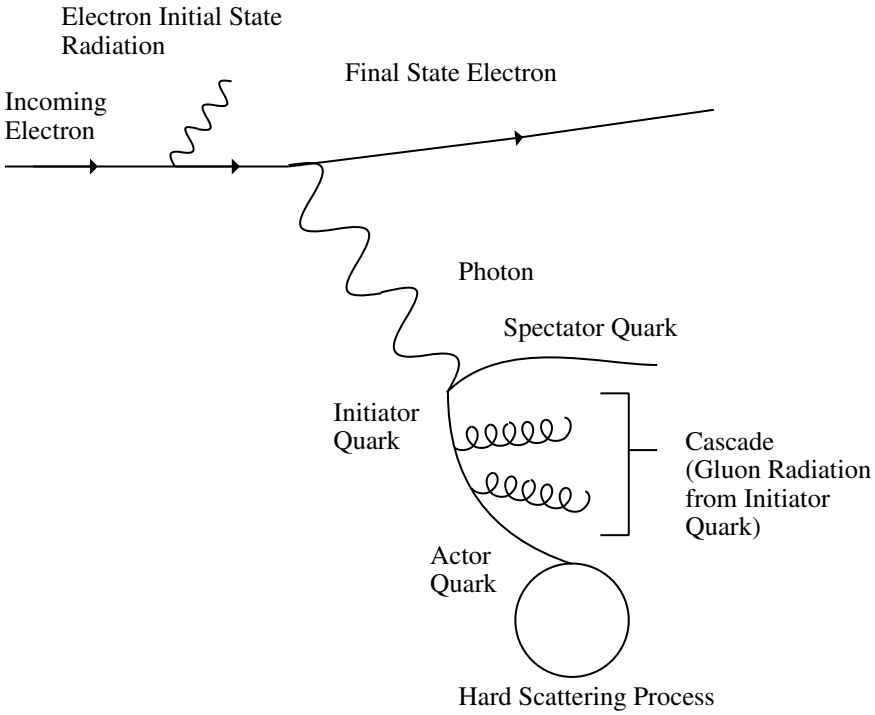

Figure 6.1: The electron side of a HERA resolved photoproduction event.

In chapter 2, it was assumed that the photon remnant comes from the step where the initiator and spectator quarks split. However, it is clear that the detector will not be able to separate out the contribution from the gluon radiation from the initiator quark and therefore the photon remnant must be defined to include all partons from the original photon except for the parton that hard scattered. This definition, whilst not exactly equivalent to the previous one, is more meaningful when the limits of what can be reconstructed by the detector are taken into consideration.

The uncertainty in defining the photon remnant also leads to an uncertainty in defining x_γ as it is not clear whether the relevant x_γ is for the initiator quark or for the actor quark in figure 6.1. With the new definition of the photon remnant, it is clear that the appropriate x_γ is that of the actor quark. This is the x_γ that can be reconstructed from the final state jets and also has the required property that

$$x_\gamma + x_{rem} = 1$$

where x_{rem} is the fraction of the incoming photon's four-momentum taken by the photon remnant

(according to the new definition).

The purpose of this study was to compare data with Monte Carlo predictions rather than to extract absolute cross-sections. Therefore, no attempt has been made to unfold any measurements back to the parton level. Also, the errors shown in all plots in this chapter are statistical only as no attempt has been made to evaluate the systematic errors.

Data Sets

A) Photoproduction Pre-selection

For the 1992 data, runs were assigned a quality flag of good (where all subdetectors were available), medium (where the central tracking, calorimetry and electron tagger were fully functioning) or poor (where a critical subdetector was unavailable). A sample of electron tagged photoproduction candidates has been selected for analysis using only good and medium runs, corresponding to an integrated luminosity of 23.8 ± 1.5 nb^{-1}. From this data sample, a pre-selection of events taken with the ETAG*t0 trigger has been made. This trigger requires an electron candidate in the electron tagger (with an energy greater than 4 GeV), no photon in the photon tagger (i.e. less than 2 GeV deposited in the photon tagger) and at least one track in the MWPCs of the central tracker. In addition to this trigger requirements, cuts were made to reduce the number of background events, as described in the 'Data Selection' section. The resulting pre-selection contained 4927 events.

B) Simulation

The PYTHIA 5.6 generator [60] was used to to compare theoretical predictions with the data. The structure function used for the photon was the leading-order parameterisation of GRV [27] contained in PDFLIB [61]. The proton structure function used was the MRSD0 parameterisation [62].

The first stage of the generation procedure used was to generate the parameters of the scattered electron and photon using the Weizsacker-Williams approximation (allowing initial

state radiation from the electron). Before carrying out the rest of the generation procedure, the events were randomly accepted or discarded with a probability of acceptance equal to the tagger acceptance for the scattered electron. This was done in order to save processing time and to ensure that only events within the acceptance of the tagger were fully generated.

The events were produced using flat distributions in x_γ and x_p, with each event being given a weight based on the probability of obtaining that value of x given by the structure function parameterisations. This has the advantage of producing more events in the tails of the distribution (even though they have small weightings) and saves processing time by not generating large numbers of events in areas that are not necessarily of interest.

This method also has the advantage that different parameterisations of the structure functions may be considered by reweighting the events, avoiding additional Monte Carlo production. However, care must be taken when comparing the predictions of the two different structure function parameterisations as reweighting the same events leads to correlations between the statistical fluctuations in the two predictions. The structure function parameterisation chosen for the reweighting was the LACIII set [25]. This was chosen because it differs significantly from the GRV parameterisation used in generation. Hence, a comparison of the two predictions indicates whether or not the current level of statistics is sufficient to distinguish between alternative structure function parameterisations.

The events generated by the above method were passed through full detector simulation (using H1SIM) and reconstruction (using H1REC). These events were then subject to the same cuts as the data. It was assumed that the trigger efficiencies for the data and Monte Carlo were the same. The sum of the event weights generated before acceptance considerations corresponded to an integrated luminosity of 244.4 nb^{-1}. A scale factor of 0.0974 was therefore applied to the weighted sample in order to compare absolute Monte Carlo predictions with the 23.8 nb^{-1} of data collected in 1992. Applying the acceptance and pre-selection cuts resulted in a Monte Carlo pre-selection of 6744 events.

C) Proton Pilot Bunch Data

Most of the background for photoproduction events is expected to come from a coincidence of a fake electron tagger signal with a proton induced background interaction inside the H1 detector. In the Autumn 1992 run, HERA ran with two pilot bunches, one for the electrons and one for the protons. These pilot bunches had no counterpart in the other beam so interactions produced by these bunches were purely background events. A sample of 3949 proton beam induced background events was prepared and inspected to ensure efficient background rejection. It was not possible to scale the pilot bunch sample up with the luminosity to predict the background as the background rates scale with proton beam intensity and vacuum conditions. It has been assumed in this analysis that the properties of beam induced interactions were similar for pilot and interacting bunches (despite the slightly different conditions encountered by these non-interacting bunches). Using this assumption the proton pilot bunch data may be used to estimate the background contamination in the data sample.

Data Selection

In 1992, the H1 detector was still in the early stages of its operation and some subdetectors were unreliable, poorly treated by reconstruction or not fully instrumented. For this reason, the forward tracker, the instrumented iron calorimetry and the plug were excluded from the analysis. In addition, tracks in the central tracking detector were required to have at least 10 hits in the CJC or 3 in the BPC, lie within the range $5.0° < \theta < 175.0°$ and have a distance of closest approach to the beam axis of less than 2 cm. Tracks were further required to have values of χ^2 from the vertex fit of less than 10,000, a start radius of less than 30.0 cm and to start less than 50.0 cm from the event vertex.

The clustering algorithm used in the calorimetry was not fully reliable in Autumn 1992 so the calorimeter cell information, corrected for dead material, was used for energy flow measurements. Noisy cells with a deposited energy of less than 0.1 GeV in the liquid argon (0.6 GeV for the BEMC) were rejected. The main calibration studies for the BEMC have been

concerned with electromagnetic energy deposition. Monte Carlo studies [63] indicate that a scale factor of 1.6 should be applied when using the BEMC to measure hadronic energy. This factor was applied after the noise cut.

Samples taken with the ETAG*t0 trigger were expected to be relatively free of background. However, background events may be accepted by the trigger if a proton beam-gas interaction occurs inside the H1 detector region while an electron beam-gas or beam-wall interaction scatters an electron into the tagger. In addition to this background, events with beam halo muons in the detector and events with a cosmic ray passing through the detector must also be rejected. For some of the Autumn 1992 data, there was coherent noise in the liquid Argon calorimetry which makes some individual events unuseable.

Standard H1PHAN routines [49] were used to reject cosmic ray, beam halo and coherent noise contaminated events by insisting that there be no cosmic ray muon found, no coherent noise found and that the energy deposited in the calorimeters from beam halo muon candidates be less that 7.5 GeV.

As discussed in chapter 3, the acceptance of the electron tagger covers the range $0.2<y<0.8$ so no photoproduction event accepted by the ETAG*t0 trigger should have a value of y outside this range. Hence, it was insisted that the energy of the electron detected in the electron tagger must lie between 8 GeV and 20 GeV (corresponding to $0.25 < y < 0.7$). Figures 6.2(a) and (b) show the energy spectrum in the tagger for data and GRV Monte Carlo before this cut, which was made on the pre-selection. The shape of this distribution is essentially governed by the acceptance of the electron tagger. The differences between the data and Monte Carlo prediction arise from the fact that the Monte Carlo acceptance is unsmeared by resolution at this stage and the ETAG*t0 trigger conditions have yet to be imposed upon the Monte Carlo.

Figure 6.2: Electron tagger energy spectrum before applying cuts for a) data, b) GRV Monte Carlo.

It was further insisted that a primary vertex be reconstructed and that the vertex be within the fiducial interaction region of -44.0 cm $< z_{vertex} <$ 44.0 cm. This cut was imposed in order to reduce the number of events from proton beam-gas interactions. Losses due to this cut have been determined by the photoproduction group to be (12±2)% using a track independent trigger [64]. Figures 6.3(a) and (b) show the distribution of the vertex in z for data and GRV Monte Carlo respectively before applying this cut. Figure 6.3(c) shows the distribution of the vertex in z for proton pilot bunch data. The large peak at zero in this figure, which extended to 1440, is shown truncated. This peak corresponded to events where no good vertex was reconstructed. The distribution was found to extend further in z for the pilot bunch than for the data, as expected. The actual distribution of pilot bunch events was expected to be flat, but this was modulated by the acceptance and efficiency of the central tracking chambers which varies with z. From figure 6.3(c) it was estimated that 50% of proton pilot bunch events have a good reconstructed vertex within the fiducial region.

Figure 6.3: distribution of z_{vertex}, the z position of the primary reconstructed vertex before applying cuts for a) data, b) GRV Monte Carlo, c) Proton pilot bunch.

To tag events with a hard scatter, the scalar sum of the transverse energy in the event was required to be above 10 GeV. The transverse energy, E_T, of a particle is defined as

$$E_T = E \frac{p_T}{p}$$

where E is the energy of the particle, p is the magnitude of the particle's momentum and p_T is the component of the particle's momentum transverse to the beam direction. The total transverse energy was evaluated using calorimeter cells with $\theta > 0.1$ radians (i.e. excluding the very forward region).

In order to reject the remaining background, a cut was made on y_{hadron}, the value of y calculated by the Jacquet and Blondel method [65] from the hadronic final state, utilising the energy flow information from the calorimeter. This gives

$$y_{hadron} = \sum_{j=1}^{\#hadrons} \frac{\left(E_j - p_{zj}\right)}{2E_e}$$

where E_j and p_{zj} are the energy and z-component of momentum for hadron j and E_e is the energy of the incoming beam electron. This method is insensitive to losses down the beam pipe. For real photoproduction events, the value of y_{hadron} calculated by this method should agree with that calculated from the electron tagger and should at least lie within the electron tagger acceptance.

Figure 6.4 (a) shows the distribution of y_{hadron} for the data, 6.4(b) for the Monte Carlo. The data distribution was found to have a peak in the region 0.0 to 0.1 which was absent from the Monte Carlo. However, the distribution for the proton pilot bunch events, shown in figure 6.4(c), showed a sharp peak below 0.1. This suggested that the peak in data was due to contamination from events with an interaction in the centre of H1 similar to those induced by the proton pilot bunch. Figures 6.5 (a) and (b) show that the values of y calculated from the hadronic information and from the electron information are correlated for both data and Monte Carlo.

Figure 6.4: y_{hadron} calculated by the Jacquet-Blondel method before applying cuts for a) data, b) GRV Monte Carlo, c) Proton pilot bunch.

Figure 6.5: correlation plot of $y_{electron}$ against y_{hadron} after mini-DST selection (y_{hadron}>0.1) for a) data, b) GRV Monte Carlo.

When producing the pre-selection it was insisted that y_{hadron}>0.1. Only those calorimeter cells at θ>0.1 radians were used in calculating the value of y_{hadron} in order to avoid possible problems from including part of the proton remnant in the measurement. The peak below 0.1 in the pilot bunch data contained 3084 events (78.1±0.6% of the total). By scaling this peak to the 90 events below 0.1 in the data the total number of proton beam induced background events in the data sample was estimated to be 115.2±17.8 events.

This cut was tightened for this analysis by insisting that y_{hadron}>0.2, calculated using all calorimeter information (i.e. no θ requirement). Imposing this cut, 367 pilot bunch events remained out of 3949 (9.3±0.4%). Imposing the y_{hadron}>0.2 cut resulted in an estimated 10.7±1.7 proton beam induced background events. It was not clear whether these events were distributed in z in the same way as the proton pilot bunch events as the acceptance varies with z. If they were, the z_{vertex} cut would reduce the background by a further 50% to 5.4±0.9 events. No further attempt was made to treat the remaining background in the sample.

After imposition of these cuts, 4354 events remained from the pre-selection, compared with predictions of 5957 events from the GRV Monte Carlo and 10915 events from the LACIII reweighted Monte Carlo.

The Jet Finding Algorithm

In order to examine the properties of the photon remnant, events with two jets from the hard scattering process were selected to ensure clean event identification. The jet algorithm used was the LUCELL cone algorithm [66]. This algorithm uses pseudo-rapidity, η, defined as

$$\eta = -\ln\left(\tan\frac{\theta}{2}\right)$$

where θ is the angle between the particle's momentum vector and the proton beam direction. This is an approximation to rapidity, j, which is given by

$$j = \frac{1}{2}\ln\left(\frac{E + p_z}{E - p_z}\right)$$

for a particle with energy E and z-component of momentum p_z. Intervals in both rapidity and ϕ are invariant under boosts along the beam axis.

A grid was defined in $\eta-\phi$ space which was then filled with the transverse energy information from the calorimeters. The grid used had 24 cells in ϕ and 25 in η, in the range $-2.5 < \eta < 2.5$. A search was made for an initiator cell with a transverse energy, E_T, of $E_{Tini} \geq 0.2$ GeV. All cells satisfying this cut, starting with the cell with the highest E_T, were then used as the centre of a cone of radius R = 1.0. If the transverse energy within this cone was greater than a threshold, E_{Tmin}, of 5.0 GeV the cone was accepted as a jet.

Only events with at least two jets defined in this way were accepted for further study. Figure 6.6 shows the fraction of events found with zero, one, two, three and four jets for the data, GRV Monte Carlo and LACIII reweighted Monte Carlo samples.

	Data	GRV	LACIII
Zero Jets	64.8±0.7%	68.7±0.6%	62.6±0.6%
One Jet	24.4±0.7%	26.6±0.6%	30.7±0.6%
Two Jets	8.7±0.4%	4.1±0.3%	5.7±0.3%
Three Jets	1.8±0.2%	0.5±0.1%	0.9±0.1%
Four Jets	0.3±0.1%	0.1±0.1%	0.1±0.1%

Figure 6.6: Fraction of events with zero, one, two, three and four jets in the data, GRV Monte Carlo and LACIII reweighted Monte Carlo samples.

A total of 467 data events remained after this selection. The summed weight of GRV Monte Carlo events remaining was 2836.9, corresponding to 277 events. The weight remaining in the LACIII reweighted Monte Carlo was 7470.3 corresponding to 728 events. Hence, the fraction of two jet events was found to be higher in the data than in either of the Monte Carlo predictions. The absolute predictions for the number of events were found to bracket the data, the GRV predicting fewer events and the LACIII predicting more. With the low value of E_{Tmin} chosen, the presence of noise may have been a significant factor in raising jet energies above threshold. However, a low threshold was necessary in order to find a significant number of two jet events with the small integrated luminosity available. The number of jets was also increased by a difference in forward energy flow between the data and Monte Carlo. This is discussed in the section entitled 'Differences In Energy Flow In The Forward Region Between Data And Monte Carlo Predictions'.

Having established the difference in the number of events after cuts in data and the two Monte Carlo predictions, it is useful to compare the shapes of the predicted distributions with the observed shapes. In order to do this, the area under the histograms for data and Monte Carlo were equated. The value of the area under the histogram chosen for this equalisation was 1.0 and distributions treated in this way will be referred to as 'normalised to 1.0'.

A plot of the transverse energy flow with respect to the highest E_T found in the event

was then made in order to confirm that the events selected had a genuine back-to-back structure. For each calorimeter cell in the event, a histogram entry was made at $\Delta\phi$, the difference in ϕ between the cell and the cell with the highest E_T. This entry was given a weight equal to the E_T of the cell. The plot was then normalised to 1.0 for comparison with Monte Carlo prediction. The resulting plot is shown in figure 6.7(a) and figure 6.7(b) shows a similar plot compiled using central tracks (relative to the highest E_T track). It was concluded that the events selected by LUCELL as having two jets had a clear back-to-back structure for both data and Monte Carlo.

Figure 6.7: Transverse Energy flow in ϕ with respect to the highest transverse energy in the event a) for calorimeter cells, b) for central tracks. Points are data, solid histogram is GRV Monte Carlo prediction.

After jet finding, the shapes of the distributions of electron tagger energy E_{etag}, y calculated from the electron $y_{electron}$, y_{hadron} and z_{vertex} were examined (shown in figures 6.8(a), (b), (c) and (d) respectively) in order to ensure that different biases had not been introduced into the data and Monte Carlo samples. The shapes of the electron tagger energy distributions were found to be similar although the data distribution had a longer tail at higher energies. The shapes were observe to differ less in figure 6.8 than in figure 6.2, where the trigger requirement had not

been imposed on the Monte Carlo sample. The $y_{electron}$ distribution was found to have a tail at low values which corresponded to the tail at high electron tagger energies. The data distribution was found to peak at a lower value of y_{hadron} than the Monte Carlo. The shapes of the data and Monte Carlo z_{vertex} distributions were found to be in good agreement.

Figure 6.8: Distribution for the two-jet event samples in a) electron tagger energy, b) y_{hadron}, c) $y_{electron}$ and d) position of primary reconstructed vertex in z. Points are data, solid histogram is GRV Monte Carlo prediction.

Comparisons Between Data And Monte Carlo

A) Charged Track Distributions

Figures 6.9(a), (b), (c) and (d) show the E, η, ϕ and p_T distributions respectively of charged tracks in the central tracking detector from the two-jet data and Monte Carlo samples. The shapes of data and Monte Carlo were found to agree well in E and p_T. The data was found to have a peak in the region $1<\eta<2$ which was not predicted by the Monte Carlo. This difference is not fully understood at the present time. A full discussion of this effect and other related problems will be given in the section entitled 'Differences In Energy Flow In The Forward Region Between Data And Monte Carlo Predictions'. The data distribution was also found to have a dip in the region $-3.1<\phi<-2.2$ which was not predicted by the Monte Carlo. This dip was caused by dead sectors in the central jet chamber which were not correctly treated in the Monte Carlo simulations. Further studies could ensure that these sectors are made dead for the same fraction of events as in the data.

Figure 6.9: Number of charged tracks (normalised to 1.0) in the central detector as a function of a) track energy, b) track pseudo-rapidity, c) track ϕ, d) track transverse momentum. Points are data, solid histogram is GRV Monte Carlo prediction.

B) Jet Distributions

The E, η, ϕ and p_T distributions of the jets were examined for the reconstructed jets, as shown in figures 6.10(a)-(d) (normalised to 1.0) and in figures 6.11(a)-(d) (with absolute normalisation). The shapes of the ϕ and p_T distributions were found to agree well. A peak was observed in the E distribution for the data around 25 GeV which was not present in the Monte Carlo. A caveat should be made regarding jets near the extremes of the η range used ($-2.5<\eta<2.5$) as the truncation of jets may have unpredictable results if the jet shapes in data and Monte Carlo differ. However, even taking this into consideration, the shape of the data η distribution was observed to be different from either of the two Monte Carlo predictions, having a peak in the forward region, $1<\eta<2$.

Figure 6.12 shows that the jets in the E peak (i.e. with 16 GeV < E < 24 GeV) lie predominantly in the η peak also. The presence of these jets is thought to be related to the effects observed in the charged track distributions and will be discussed later.

Figure 6.10: Number of jets (normalised to 1.0) as a function of a) E, b) η, c) ϕ and d) p_T. Points are data, solid histogram is GRV Monte Carlo prediction, dotted histogram is LACIII reweighted Monte Carlo prediction.

Figure 6.11: Number of jets (absolute normalisation) as a function of a) E, b) η c) ϕ and d) p_T. Points are data, solid histogram is GRV Monte Carlo prediction, dotted histogram is LACIII reweighted Monte Carlo prediction.

Figure 6.12: Number of jets as a function of η for all jets in the data (solid histogram) and those jets with energies in the range 16 GeV < E < 24 GeV (points).

C) Jet Profiles

A jet profile is defined as the distribution of E_T with respect to the centre of the jet. These profiles were compiled by considering all tracks or calorimeter cells within the jet and making an entry in the profile histogram at the appropriate position, weighted by the E_T of the track or cell. The distributions were then normalised to 1.0 for shape comparison. Figure 6.13(a) shows the jet profile using calorimeter cells in $\Delta\eta$, the difference between the cell η and the η of the centre of the jet. Both the data and Monte Carlo jets were found to be centred at zero, but the data distribution was seen to be broader than the Monte Carlo prediction. The data distribution was also found to contain more transverse energy in the forward ($\Delta\eta$ positive) jet tail than in the negative jet tail.

This effect has also been reported in an H1 paper [64], where it was found that the effect was observed for jets in the region $0.5<\eta<1.5$ but not for those in the range $-1.5<\eta<0.5$. The contribution was found to be almost independent of jet energy but to rise with the jet η. The jet studies in [64] used a sliding-window algorithm requiring $E_T>7.0$ GeV rather than LUCELL to find jets. However, as the cone size used was R=1.0, the results are expected to be applicable to jets found with LUCELL. The majority of the jets found in this study were observed to lie in the forward region, so the observed difference in jet profiles between data and Monte Carlo is consistent with that reported in the paper. This effect will be discussed more fully in the next section. Figure 6.13(b) shows the jet profile from calorimeter cells in $\Delta\phi$, the difference between the ϕ of the cell and the ϕ of the centre of the jet. The data distribution was found to be broader than the Monte Carlo prediction but was symmetric about zero.

The jet profiles were also examined using central tracks. As shown in figures 6.13 (c) and 6.13 (d), the data and Monte Carlo distributions were found to be in agreement within errors for both η and ϕ. The large errors on some points in these distributions resulted from the inclusion of a small number of tracks with high E_T.

Figure 6.13: Jet transverse energy profiles, normalised to 1.0, for a) calorimeter cells in η, b) calorimeter cells in ϕ, c) central tracks in η and d) central tracks in ϕ. Points are data, solid histogram is GRV Monte Carlo prediction.

Differences In Energy Flow In The Forward Region Between Data And Monte Carlo Predictions.

As described above, significant differences were found between the data and the PYTHIA Monte Carlo distributions using either the GRV or LACIII photon structure function parameterisations. These difference were:

1) That a higher fraction of the data events had two or more jets than predicted by the Monte Carlo.

2) That more tracks were observed in the forward region, $\eta>1$, for data than for Monte Carlo.

3) That more jets were found in the forward region for data than for Monte Carlo.

4) That the jet tails showed an excess of energy in the forward region over that predicted by the Monte Carlo shape. This effect has also been reported in an H1 paper [64].

If the last difference were not observed, a modification of the structure function parameterisation might be able to account for the differences. However, the difference in the jet tails may not be easily explained by making such a modification. It is currently thought that there is more energy in the forward region in data than is predicted by Monte Carlo and that this energy is spread evenly in ϕ within each event ([67] and [68]). This presents a serious problem.

Consider a jet with 4.5 GeV of transverse energy. If this jet were to be scattered into the barrel region, the reconstructed transverse energy would only be 4.5 GeV and the jet would therefore not be tagged by LUCELL. However, if the jet were to be scattered into the forward region, the transverse energy in the LUCELL cone would be the sum of the jet transverse energy and whatever 'extra' transverse energy is present from the evenly-distributed energy flow. If this energy were large enough, the reconstructed transverse energy would be raised above the 5 GeV threshold. This would mean that the jet would now be identified by LUCELL. Therefore, the presence of such energy would result in a larger number of jets being identified in the forward region for data than was predicted by Monte Carlo, despite agreement in the backwards region. This explanation fits the observations described above.

The only way to disentangle the difference in jet rates arising from an inaccurate

structure function parameterisation from a difference in jet rates caused by this threshold effect is to understand and correctly reproduce the energy flow in the forward region. It is currently suggested that, as the data and Monte Carlo distributions match well except for $\eta>1$, there is some physical effect spraying extra particles into the forward part of the detector. However, this has not yet been substantiated. Therefore, any conclusions regarding energy flow, jet rates and photon structure function parameterisations must be treated with a degree of caution, especially in this forward region.

Work is in progress at DESY to understand this effect using both the 1992 data and the new 1993 data for which the forward tracker is fully operational and well reconstructed. Several possibilities are being explored, including:

1) That the model used thus far of one hard scatter per event may be inadequate and that the possibility of multiple partonic interactions occurring in the same event may have to be considered [69]. Preliminary studies [70] indicate that such models may be able to explain the effect.

2) That the fragmentation model used thus far, JETSET [71], may be inappropriate or improperly tuned. Studies are also in progress using the HERWIG [72] and ARIADNE [73] models to investigate the effects of the fragmentation model on the Monte Carlo predictions.

3) That there may be some instrumental or experimental effect spraying particles into the forward region. For example, some dead material around the beam-pipe may be absent or wrongly described in the simulation program.

4) The fragmentation of the proton remnant may not be correctly described by PYTHIA. This may result in the fragments of the proton being spread over a wider range in η than in the Monte Carlo prediction, thus supplying the extra energy.

The x_γ Distribution

The value of x_γ may be calculated from the reconstructed parameters of the two jets using the method described in appendix A. If both jets are in the forward region, $\eta>1$, a low value of x_γ results. The distribution of x_γ obtained by using the jet information with absolute normalisation is shown in figure 6.14(a) and normalised to 1.0 in figure 6.14(b). Although the GRV Monte Carlo prediction was observed to be in agreement with the data above x_γ=0.3, the data distribution was found to have a pronounced peak at lower values of x_γ. This was expected given the difference between the data and Monte Carlo jet η distributions. The LACIII reweighted prediction was found to be significantly higher than the data for x_γ>0.3 and also did not show a peak at lower values of x_γ. Both Monte Carlo predictions showed a peak at x_γ=0.6 which was not seen in the data. Inspection of the Monte Carlo events led to the conclusion that this peak was due to three events with high weights, illustrating the problem caused by the correlation in statistical fluctuations when reweighting the Monte Carlo events.

Figure 6.14: Number of events as a function of x_γ calculated from jets, a) absolute normalisation, b) normalised to integral 1.0. Points are data, solid histogram is GRV Monte Carlo prediction, dotted histogram is LACIII reweighted Monte Carlo prediction.

Photon Remnant Algorithm

Using the LUCELL algorithm for jet finding, some of the energy deposited in the calorimeter is tagged as coming from the hard scattered partons. The remaining energy in the event must have come from somewhere, so an algorithm to collect the rest of the cells should in principle give the sum of the photon and proton remnants. However, the radius R = 1.0 described in the Jet Finding section may not fully contain the jets and jet tails, noisy cells and pedestals under the jets may also contribute to energy outside the jet cones. Therefore, a limited range of η-ϕ space should be summed to define the photon remnant. As the photon remnant is predicted to be mostly in the backward region and the proton remnant mostly in the forward region, separation of the two remnants should be possible.

The first study of this kind of collection algorithm was carried out by D'Agostini and Monaldi on Monte Carlo datasets [74]. This work examined the possibility of using the amount of energy in a cone one unit in η behind the backwards-most jet as a discrimination between resolved and direct events. D'Agostini and Monaldi found that good discrimination should be possible by searching for at least 3 GeV of energy in this backwards cone. One approach to finding the photon remnant is therefore to sum all particles in this cone and examine the properties of the entity so formed. The region $\eta-\phi$ space summed by this algorithm is illustrated in figure 6.15. This algorithm will be referred to as the D/M algorithm, although they only used it to discriminate between direct and resolved events rather than to define the remnant.

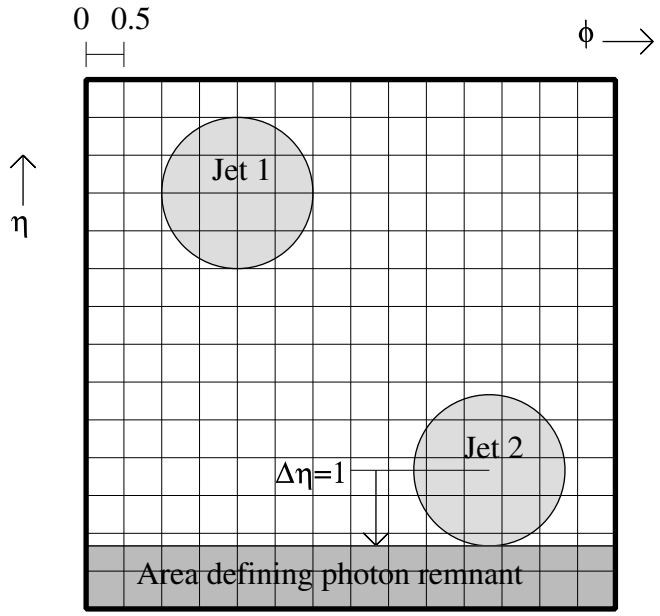

Figure 6.15: The D/M algorithm for defining the photon remnant based on the cone defined by $\Delta\eta=1$.

This algorithm has the advantage of not assuming the presence of a photon remnant in order to find it. Alternative algorithms based on event decomposition may not be used to simply demonstrate the existence of a photon remnant because such routines are always controlled by a cut-off parameter which limits the level of decomposition. The presence of a remnant does not depend on any such arbitrary parameter and it is therefore advantageous to use a simpler algorithm in this initial study to demonstrate the existence of the remnant.

Such an algorithm has the disadvantage of only catching the remnant when it is within this $\Delta\eta=1$ cone and there is no reason to suppose that the remnant is always fully contained within this area. In addition to examining the data with the D/M algorithm, a broader algorithm was devised to find the photon remnant when it is not contained entirely behind the backwards-most jet. The algorithm chosen is shown pictorially in figure 6.16.

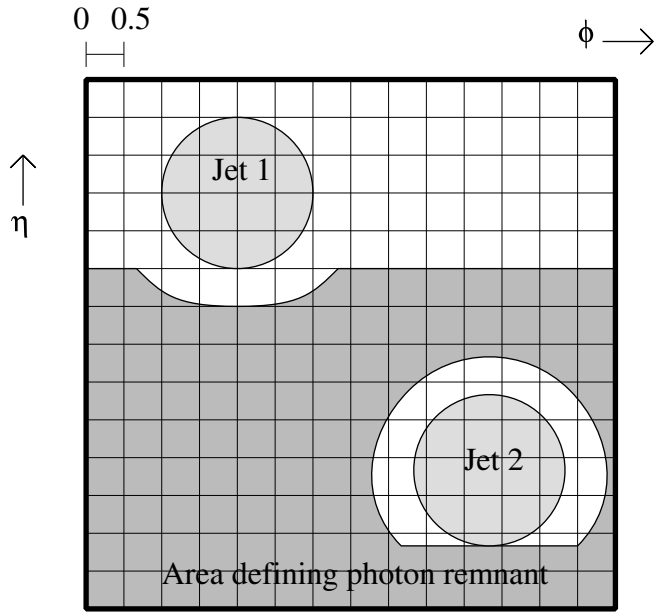

Figure 6.16: The alternative ('new') collection algorithm for defining the photon remnant.

The area included in this second algorithm is defined by the following criteria:

1) Anything at least one unit in η behind the backward most jet is included.

2) Anything at least one unit in η behind the forward most jet and at least a distance $\Delta R=1.5$ units from the centre of the nearest jet.

This algorithm has the advantage of being able to pick up the photon remnant when it is well separated in ϕ from the backward most jet but is at a similar value of η. However, as the area included is larger than for the first algorithm the problems arising from the inclusion of noise and jet tails are expected to be more severe than for the first algorithm. A further problem with both of these algorithms is that the remnant may be identified as a jet if it fulfils the jet finding criterion of $E_T>5$ GeV in a cone of radius 1.0. The performance of the algorithm on Monte Carlo simulations of the photon remnant may be used to assess the severity of these problems. However, the Monte Carlo predictions for the photon remnant must be compared with the data to ensure that such a study is meaningful. As the Monte Carlo generator used had been tuned primarily for proton-anti-proton collisions rather than electron-proton collisions, some differences are expected.

Photon Remnant Results

A) Fraction Of Events With A Photon Remnant

In data, using the D/M algorithm, a photon remnant was found in 367 out of 467 two jet events, (79±2%). In the GRV Monte Carlo, the fraction of those events with a found remnant was 65±1%. In the LACIII reweighted Monte Carlo, the fraction of events with a found remnant was 62±1%. For the new algorithm, the percentages were 96±1% for data, 88±1% for the GRV Monte Carlo and 90±1% for the LACIII Monte Carlo. It was therefore concluded that a substantial fraction of the photoproduction events collected had a remnant present and that this was indicative that a large fraction of the events were resolved, as theoretically predicted.

A greater fraction of events in the data were found to have a remnant present than in the Monte Carlo. However, the presence of a remnant is expected to be very sensitive to the presence of noisy cells and particles not assigned to a jet as one cell above the noise threshold anywhere in the $\eta-\phi$ region considered by the algorithm is sufficient to tag the event as having a remnant. This explains why a larger fraction of events were found to have a remnant when using the new algorithm as it considers an increased area of $\eta-\phi$ space and therefore there is a greater chance of using cells above threshold.

For the Monte Carlo samples, the possibility of using the presence of a remnant to discriminate between direct and resolved processes was examined. Figure 6.17 shows the percentage of events with and without a remnant for direct and resolved processes in the GRV and LACIII reweighted samples. The error on the percentages was estimated as ±2% based on the number of events. For the D/M algorithm, it was found that a reasonable discrimination was achievable based on the detection or non-detection of a photon remnant. With the new algorithm, which includes a much larger area in $\eta-\phi$ space, the discrimination was found to be poor.

For the reasons discussed above, the presence of a remnant is very sensitive to any deposition of energy from whatever source. Therefore, an energy requirement on the reconstructed remnant was imposed in order to improve the discrimination. This was the approach followed by D'Agostini and Monaldi, who required at least 3 GeV in the cone defined

by $\Delta\eta=1$ to tag an event as resolved. The fraction of events with and without a remnant of at least 3 GeV is shown in figure 6.18, again with estimated ±2% errors from the number of events.

	D/M GRV	D/M LAC	New GRV	New LAC
Resolved With	70.4%	63.9%	90.8%	90.8%
Resolved Without	29.6%	36.1%	9.2%	9.2%
Direct With	18.4%	18.4%	64.6%	64.6%
Direct Without	81.6%	81.6%	35.4%	35.4%

Figure 6.17: Percentage of direct and resolved events with and without a photon remnant as defined by the D/M and new algorithms for GRV and LACIII reweighted Monte Carlo, requiring only the presence of a remnant jet.

	D/M GRV	D/M LAC	New GRV	New LAC
Resolved With	46.7%	38.3%	61.6%	55.8%
Resolved Without	53.3%	61.7%	38.4%	44.2%
Direct With	5.9%	5.9%	44.0%	44.0%
Direct Without	94.1%	94.1%	66.0%	66.0%

Figure 6.18: Percentage of direct and resolved events with and without a photon remnant as defined by the D/M and new algorithms for GRV and LACIII reweighted Monte Carlo, requiring at least 3 GeV of energy in the found remnant.

The D/M method for discriminating between direct and resolved events was observed to perform well, discarding most of the direct events while accepting most of the resolved events. Imposing a cut of 3 GeV on the remnant energy improved the rejection of direct events to almost 95% but reduced the acceptance for resolved events to less than 50%. The new algorithm was found to be less useful in discrimination as the difference between the acceptances for direct and resolved events was not as large as for the D/M algorithm. This was due to the inclusion of more noisy cells when defining the remnant. Either algorithm could be used to provide an enriched sample of resolved events but neither could reliably be used to extract a sample of direct events based on the absence of a remnant, even with an energy cut of 3 GeV.

The fraction of two-jet events in the data with a remnant of energy of at least 3 GeV was 55±2%, compared with 42±2% for the GRV Monte Carlo and 37±2% for the LACIII reweighted Monte Carlo. With the new remnant algorithm, the fractions became 69±2% for data, 60±2% for GRV and 55±2% for LACIII. The data were observed to have larger fraction of events with a remnant than the Monte Carlo predictions, even when the 3 GeV energy requirement was imposed.

B) Photon Remnant Distributions

The distributions of the photon remnant were examined for both the D/M and new algorithms. Figures 6.19(a)-(d) show the distributions with E, η, ϕ and p_T respectively for the D/M algorithm, normalised to 1.0, figures 6.20(a)-(d) with absolute normalisation. Figures 6.21(a)-(d) and 6.22(a)-(d) show the distributions for the new algorithm with normalisation 1.0 and absolute normalisation respectively. With the D/M algorithm, good agreement between the shapes of the data and Monte Carlo E distributions was observed and reasonable agreement was found in η and ϕ. The data distribution was found have a larger fraction of events with $\eta>0.0$ than predicted by the Monte Carlo. A peak was found at $\phi=2.5$ in the Monte Carlo distributions but investigation revealed that this was due to one event with high Monte Carlo weight. The data and Monte Carlo p_T distributions were found to agree in the region $p_T>2$ GeV but below this the data distribution was found to be peaked whereas the Monte Carlo prediction fell smoothly.

With the new algorithm, the Monte Carlo predictions for the shapes of the distributions in E, η, ϕ and p_T were found to be in agreement with the data. The single event with high Monte Carlo weight that had given a peak at $\phi=2.5$ with the D/M algorithm was reconstructed to have a remnant at $\phi=-2.75$ by the new algorithm, producing a peak at this value.

The distributions for both algorithms fell sharply with p_T and no remnants were observed with $p_T>6.0$ GeV. It was suggested that remnants with higher p_T might have been labelled as jets by LUCELL if the transverse energy of the jet were sufficiently well-collimated as to exceed the 5 GeV threshold in any one cone of radius 1.0 in $\eta-\phi$ space.

Figure 6.19: Number of photon remnants (normalised to 1.0) defined by D/M algorithm as a function of a) E, b) η, c) ϕ, d) p_T. Points are data, solid histogram is GRV Monte Carlo prediction, dotted histogram is LACIII reweighted Monte Carlo prediction.

Figure 6.20: Number of photon remnants (absolute normalisation) defined by D/M algorithm as a function of a) E, b) η, c) ϕ, d) p_T. Points are data, solid histogram is GRV Monte Carlo prediction, dotted histogram is LACIII reweighted Monte Carlo prediction.

Figure 6.21: Number of photon remnants (normalised to integral 1.0) defined by new algorithm as a function of a) E, b) η, c) ϕ, d) p_T. Points are data, solid histogram is GRV Monte Carlo prediction, dotted histogram is LACIII reweighted Monte Carlo prediction.

Figure 6.22: Number of photon remnants (absolute normalisation) defined by new algorithm as a function of a) E, b) η, c) ϕ, d) p_T. Points are data, solid histogram is GRV Monte Carlo prediction, dotted histogram is LACIII reweighted Monte Carlo prediction.

C) Photon Remnant Profiles

The transverse energy profiles of the photon remnant in η and ϕ were obtained by the method described in the 'Jet Profile' section. Profiles were obtained using both calorimeter cells and central tracker tracks. Figures 6.23(a)-(d) show the profiles for the D/M algorithm; figures 6.24(a)-(d) for the new algorithm. Good agreement was observed between Monte Carlo predictions and the data profiles.

The observation of peaks in all distributions suggested that concentrations of both calorimeter energy and tracks had been found around the axes of the found remnants, implying the presence of genuine photon remnant jets. The observation of peaks using tracks provided evidence that the found remnants were not due random concentrations of noisy cells in the calorimeter. However, the low track multiplicity in the remnant (discussed in the following section) means that a peaked shape is to be expected when the differences between the directions of the individual tracks are compared with the direction of their four-vector sum.

As described in the 'Jet Profile' section, jets found by LUCELL were observed to be well collimated and were well contained within a cone of radius 1.0 in $\eta-\phi$ space. The photon remnants found by both the D/M and new algorithms were found to be less well collimated, which could be due to the lower p_T of the remnants compared with the jets.

Figure 6.23: Photon remnant transverse energy profiles as defined by D/M algorithm, normalised to 1.0, for a) calorimeter cells in η, b) calorimeter cells in ϕ, c) central tracks in η, d) central tracks in ϕ. Points are data, solid histogram is GRV Monte Carlo prediction.

Figure 6.24: Photon remnant transverse energy profiles as defined by new algorithm, normalised to 1.0, for a) calorimeter cells in η, b) calorimeter cells in ϕ, c) central tracks in η, d) central tracks in ϕ. Points are data, solid histogram is GRV Monte Carlo prediction.

D) Distribution Of Tracks Inside The Photon Remnant

The distributions of tracks inside the remnant were found to be in good agreement in η and p_T for the D/M algorithm as shown in figures 6.25(b) and (d) respectively. However, the E distribution for the D/M algorithm (shown in figure 6.25(a)) was observed to fall more rapidly for the data than predicted by Monte Carlo. A dip in the data ϕ distribution, shown in figure 6.25(c), was observed and was found to be due to dead sectors in the central jet chamber, as described in the 'Charged Track Distribution' section. For the new algorithm, good agreement was found in E, η, and p_T, as shown in figures 6.26(a), (b) and (d) respectively. The dip in data ϕ distribution was also observed in the new remnant distribution as shown in figure 6.26(c).

Figure 6.27(a) shows the multiplicity of charged tracks found in the remnant for the D/M algorithm, figure 6.27(b) for the new algorithm. As expected from the larger collection area, the mean multiplicity is higher for the new algorithm than for the D/M. The mean multiplicity is predicted well by the Monte Carlo but the shapes of the distributions differ somewhat.

Figure 6.25: Number of central tracks (normalised to 1.0) inside photon remnant as defined by D/M algorithm as a function of a) E, b) η, c) ϕ, d) p_T. Points are data, solid histogram is GRV Monte Carlo prediction.

Figure 6.26: Number of central tracks (normalised to 1.0) inside photon remnant as defined by new algorithm as a function of a) E, b) η, c) ϕ, d) p_T. Points are data, solid histogram is GRV Monte Carlo prediction.

Figure 6.27: Number of charged tracks per event (absolute normalisation) for a) D/M and b) new remnant algorithms. Points are data, solid histogram is GRV Monte Carlo prediction, dotted histogram is LACIII reweighted Monte Carlo prediction.

E) Remnant-Jet Correlations And The $x_\gamma + x_{rem}$ Checksum

Having obtained a reconstructed remnant and a value of x_γ from the reconstructed jets, a check was made to see whether there was any relationship between the two. Plots were made of x_γ against the energy of the reconstructed remnant. The plots for the D/M algorithm are shown in figures 6.28(a) and (b) (for data and Monte Carlo respectively) and for the new algorithm in figures 6.29(a) and (b). As the energy of the remnant varies approximately as $(1–x_\gamma)$, it was expected that the energy of the remnant would be highest when x_γ was lowest. It was concluded from these plots that there was a correlation between the energy of the remnant and value of x_γ. With the D/M algorithm, the distribution for Monte Carlo events seemed to indicate that the events fell along a curve, indicating that some energy was not being reconstructed by the detector. This may be due to excluding particles at the edge of the remnant or to gaps in the calorimeter coverage. The distribution for the new algorithm was found to be more consistent with the expected scatter about a straight line.

Figure 6.28: x_γ calculated from jets versus energy of photon remnant defined by D/M algorithm for a) data b) GRV Monte Carlo.

Figure 6.29: x_γ calculated from jets versus energy of photon remnant defined by the new algorithm for a) data b) GRV Monte Carlo.

The checksum $x_\gamma + x_{rem}$ was then plotted using the jet information for x_γ and the remnant information for x_{rem} (as discussed in appendix A). The plot for the D/M algorithm is shown in figure 6.30(a) and the plot for the new algorithm in figure 6.30(b). For the D/M algorithm, the Monte Carlo predictions were in good agreement with the data, with the peak centred in the region 0.5-0.6 and peak widths approximately 0.25 found by the LOOK peak fitter. For the new algorithm, the data peak was centred at 0.68 while the Monte Carlo peaks were centred between 0.7 and 0.8. The peak widths were again found to be approximately 0.25 by the LOOK peak fitter. It was concluded that the rise in the value of the checksum in going to the new remnant algorithm was due to the inclusion of a larger area in $\eta-\phi$ space. It was not clear why the data peak, which agreed for the D/M algorithm, was found to be lower than the Monte Carlo predictions for the new remnant algorithm.

As four-momentum conservation requires $x_\gamma + x_{rem}=1$, the energy in the events does not appear to have been correctly reconstructed. As the formula for x_γ using the jet information is

mainly dependant on the rapidity values of the two jets, missing energy in the jet reconstruction would not be expected to lower the checksum value significantly so long as the jet direction is well reconstructed. The difference between the rapidity and pseudo-rapidity is negligible (approximately 2% for a particle with mass 1 GeV, momentum 10 GeV and θ=20°) and could not account for the shortfall (that is, the shift of the peak from 1.0 to lower values) in the checksum.

Missing energy in the remnant reconstruction would be expected to have a more serious effect and it was suggested that poor backward hadronic calorimetry could be responsible for the shortfall in the checksum. Inclusion of the instrumented iron calorimetry in the region should improve the situation despite the large amount of dead material between the BEMC and iron. An upgrade to the backward calorimetry is also planned.

Figure 6.30: $x_\gamma + x_{\text{remnant}}$ checksum for a) D/M b) new algorithms. Points are data, solid histogram is GRV Monte Carlo prediction, dotted histogram is LACIII reweighted Monte Carlo prediction.

Relation to the Parton Level

Because of the difficulty of disentangling the remnant reconstruction and the jet reconstruction when examining the $x_\gamma + x_{rem}$ checksum, a study was made of how well the reconstructed entities represented the parton-level kinematics. In order for this to have any meaning, the Monte Carlo predictions must be in good agreement with the data. As described in preceding sections, the agreement between the Monte Carlo and the data was found to be far from perfect. However, it was concluded that the predictions were at least to the right order of magnitude and that the disagreements were connected with a discrepancy in the energy flow in the forward direction, $\eta > 1.0$. The studies were therefore carried out, but a caveat must be made that they were made using an imperfect Monte Carlo and any conclusions drawn from them must be treated with caution.

A problem when comparing partons with reconstructed entities is how to relate the two. One way of doing this would be to go through and check all the mother-daughter relationships. However, this may introduce some problems as it is not known a priori which entity corresponds to which parton in the data. Therefore, the same method of mapping the found entities back to the parton level must be used based purely on the reconstructed information. In this study, the two jets with the highest E_T were assigned to the two partons that hard scattered. Any other jets in the event were neglected and the photon remnant was then reconstructed from the energy not contained in any of the jets. This was then assigned to the photon remnant at the parton level. In order to be consistent, the same mapping was used when comparing the reconstructed Monte Carlo events with the parton level. The only additional information used was that the two highest E_T jets were assigned to the individual hard scattered partons on the basis of closeness in $\eta - \phi$ space.

In order to check that the reconstructed values relate to the partonic values, correlation plots of reconstructed value versus generated value were made. Ideally, all the points should lie on the diagonal and would have $(value)_{rec} = (value)_{gen}$.

Figures 6.31(a)-(d) show the correlation plots in E, η, ϕ and p_T respectively for the hard scattered partons that were reconstructed as jets. The low cut-off observed in the reconstructed E

and p_T distributions is expected as the jets were required to have at least 5 GeV of transverse energy. It was concluded that the jet reconstruction was functioning well and that the reconstructed jet parameters related back well to the parameters of the original partons.

Figure 6.31: Reconstructed parameters versus generated parameters for jets in GRV Monte Carlo: a) E, b) η, c) ϕ, d) p_T.

Figures 6.32(a)-(d) show the correlation plots in E, η, ϕ and p_T respectively for the photon remnant parton and the photon remnant reconstructed by the D/M algorithm; figures 6.33(a)-(d) for the new algorithm. It was observed that the reconstructed energy was usually significantly lower than the generated energy. This observation supports the hypothesis that the shortfall in the x_γ+x_{rem} checksum is related to missing energy in the photon remnant reconstruction. No significant improvement in the energy reconstruction was observed in going to the new remnant algorithm. The values of p_T reconstructed by both algorithms was found to be un-correlated with the generated p_T.

Figure 6.32: Reconstructed parameters versus generated parameters for photon remnant defined by D'Agostini/Monaldi algorithm in GRV Monte Carlo: a) E, b) η, c) ϕ, d) p_T.

Figure 6.33: Reconstructed parameters versus generated parameters for photon remnant defined by new algorithm in GRV Monte Carlo: a) E, b) η, c) ϕ, d) p_T.

It was therefore concluded that the reconstructed photon remnant did not relate back well to the parton level and that no improvement was observed using the new algorithm. Three possible reasons for the poor performance were suggested. Firstly, the algorithm photon remnant signal might not be resolvable above the noise level in the calorimeters, a hypothesis not supported by the observation of peaks in the photon remnant profiles. Secondly, the poor hadronic energy measurement in the backwards direction mentioned in the $x_\gamma+x_{rem}$ checksum section could be responsible. Lastly, the remnant could be picked up as a jet when it had $E_T>5$ GeV, as mentioned in the 'Photon Remnant Distributions' section. As the collimation of jets increases with increasing E_T, those remnants with E_T above threshold could also have been those which were sufficiently well collimated to be tagged by LUCELL. This would go some way to explaining why the observed p_T correlation was so bad: if the remnant had already been tagged as jet, the entity defined by the algorithms would not have been expected to relate to the parton level photon remnant.

In order to clarify which, if any, of the above suggestions was responsible for the poor performance of the remnant algorithm in relating back to the parton level, a set of 100 Monte Carlo events with total weight 84.21 were scanned with the reconstructed jet and remnant being displayed in addition to the partonic level information. The relatively small number of events gives an approximate error on the following percentages of ±10%.

In 92% of the weighted events, at least one jet corresponded to one of the hard scattered partons, the other 8% of events having no clear relationship between any of the partons and the reconstructed entities. In 49% of the events, a second jet corresponded well to the other parton. In 3% of the events, the second jet corresponded to the photon remnant parton and in 2% it was ambiguous whether the second jet or the remnant aligned better with the photon remnant parton. In the remaining 46% it was unclear to what the second jet corresponded. A third jet was found in 15% of events. For 3% of the events, the third jet clearly corresponded to the photon remnant parton and it was ambiguous whether the remnant or jet matched the remnant parton in 2% of events. In the remaining 10%, there was no visible relation between the third jet and a parton.

The remnant, defined in this instance using the new algorithm, corresponded to the

photon remnant parton in 52% of the events. In 3% of the events, the photon remnant algorithm had clearly picked up one of the hard scattered partons and in 4% it was ambiguous whether a jet or the remnant corresponded to the remnant parton. In the remaining 41% of the sample it was unclear to what the found photon remnant corresponded. The two jets and the photon remnant were all correctly identified in 44% of the events.

It was therefore concluded that the reconstruction was correctly assigning the partons in approximately 50% of the events. The photon remnant was tagged as a jet in about 10% of the events, and the remnant algorithm picked up a hard scattered parton rather than the remnant parton in only about 5% of the events.

It was therefore concluded that the detector and algorithm were both partially responsible for the poor correlation between the reconstructed and generated remnant, the result of poor hadronic calorimetry in the backwards direction and the inclusion of too many noisy cells. Future studies should examine how best to overcome these problems and how they influence the use of the photon remnant to discriminate between direct and resolved processes.

Example Event Pictures

Figure 6.34 shows a resolved photoproduction candidate as observed by H1. The jets found by LUCELL and the photon remnant found by the D/M algorithm are shown as red and blue lines respectively in figures 6.34(a) and (c). Figure 6.34(b) shows the energy deposition in the liquid argon and BEMC as a function of η and ϕ.

Figure 6.34: A resolved photoproduction candidate in the H1 detector a) *r-z* view, b) energy deposition vs. η and ϕ and c) *x-y* view. The two red lines indicate the found jet directions and the blue line the found photon remnant direction.

Figure 6.35 shows a direct photoproduction candidate as observed by H1. The jets found by LUCELL are shown as red in figures 6.35(a) and (c). No photon remnant was found for this event and there was little energy deposited in the backward region. Figure 6.35(b) shows the energy deposition in the liquid argon and BEMC as a function of η and ϕ. The large energy deposition in the forward part of the calorimeter comes from the proton remnant.

Figure 6.35: A direct photoproduction candidate in the H1 detector a) *r-z* view, b) energy deposition vs. η and ϕ and c) *x-y* view. The two red lines indicate the found jet directions.